Design and experiment of a bionic flapping wing mechanism with flapping–twist–swing motion based on a single rotation

Cite as: AIP Advances 10, 065018 (2020); doi: 10.1063/5.0008792
Submitted: 27 March 2020 • Accepted: 28 May 2020 •
Published Online: 12 June 2020

Bing Ji,[1] Qiaolin Zhu,[1] Shijun Guo,[2,a)] Fan Yang,[1] Yushuai Li,[1] Zenggang Zhu,[1] Si Chen,[3] Rui Song,[1] and Yibin Li[1]

AFFILIATIONS

[1]School of Control Science and Engineering, Shandong University, Jinan 250061, China
[2]School of Aerospace, Transport and Manufacturing, Cranfield University, Cranfield MK43 0AL, United Kingdom
[3]College of Aerospace Engineering, Nanjing University of Aeronautics and Astronautics, Nanjing 210016, China

[a)]**Author to whom correspondence should be addressed:** s.guo@cranfield.ac.uk

ABSTRACT

In the present study, a bionic flapping mechanism of a spatial six-bar configuration was designed to transform a single rotation of a motor into a three degrees of freedom "flapping–twist–swing" cooperative motion of a flapping wing. The kinematics model of the flapping mechanism movement was constructed. The flapping trajectory of the wing based on the kinematics model was to mimic the motion of a pigeon wing in landing flight. To reduce the manufacturing complexity, the flapping mechanism was simplified with only two degrees of freedom (flapping and twist) retained. Finally, a prototype model with a 0.9 m wing span was built and tested. A comparison among the experimental data, theoretical calculation results, and ADAMS simulation results revealed that the difference in the flapping and the twist amplitude between experimental observations and theoretical calculation results was 12.5% and 2.3%, respectively. This was owing to the elastic deformation of the bar and the mechanism simplification. The comparison results also indicated that the maximum difference in the inertial force was 5.9% in up-stroke and 6.7% in down-stroke, respectively. The experimental results showed that the inertial force of the model with the wing patagium was approximately 2.2 N, and the maximum positive and negative lift was 2.1 N and −1.5 N, respectively. It is hoped that this study can provide guidance for the design of bionic flapping wing mechanisms of a flapping wing aircraft for short landing flight.

I. INTRODUCTION

Flapping wing aircrafts have advantages of higher maneuverability, lower noise, and better concealment compared with fixed-wing aircrafts and rotorcrafts.[1–3] The flapping mechanism is the key module to achieve the ideal bionic performance of a flapping wing. The design of an optimal flapping mechanism with multiple degrees of freedom (DOFs) is a multi-disciplinary subject, involving mechanical, structural, aerodynamic, and bionic knowledge. The flapping motion with a single degree of freedom (DOF) cannot mimic the bionic mechanism with satisfactory performances.

Although there are a series of studies regarding the flapping mechanism in the literature, these studies mainly focus on amplifying the actuation amplitude. The planar four-bar flapping mechanism is such a typical design adopted for a microbat model.[4] The twist is achieved by the aerodynamic force acting on the flapping wing as a result of passive deformation of the wing. In this way, the twist and flapping motion cannot be coordinated by active actuation. A piezoelectric actuated flapping wing with the similar mechanism is adopted by RoboBee[5] and a line-controlled flapping mechanism by AeroVironment's Nano Hummingbird.[6] These mechanisms are capable of flapping and twist actively, but not the swing motion. Festo's Smart-Bird[7] adopts a planar eight-bar flapping wing

mechanism, which can realize flapping, twist, and folding. The twist is achieved by actively generating a wing tilt using a steering gear. However, this kind of flapping wing mechanism leads to the increase in the complexity of the control system and the aircraft's weight. Yan *et al.*,[8] Conn *et al.*,[9] and Balta *et al.*[10] use a parallel four-bar mechanism and a spatial linkage to coordinate the flapping and twist of the wing. Wang and Michael McCarthy[11] utilize a single spatial six-bar flapping wing mechanism to realize flapping and twist. The six-bar mechanism is composed of the spatial RSSR-SSS mechanisms, where R represents the revolute joint with one DOF and S represents the spherical joint with three DOFs. However, they fail to realize swing as well. The connection between the input–output linkage of the planar four-bar mechanism and the spatial linkage mechanism forms the spatial six-bar mechanism. The synthesis of the spatial six-bar mechanism mainly focuses on the control of the position and direction of the end-effector rather than the function generation. For example, Sandor *et al.*[12] design a spatial six-bar mechanism based on RSSR-SS. Chiang *et al.*[13] also take a spatial six-bar mechanism based on RSCC-RRS, where C represents the cylindric joint. Similarly, Chung[14] adopts a spatial six-bar mechanism to guide the output linkage to track the spatial trajectory.

The multi-bar mechanism can produce sufficient flapping amplitude but insufficient freedom of motion especially for safe landing of an aircraft. In this context, a flapping mechanism is developed, which can generate the flapping–twist–swing motion relying on the usual rotation of the power source. In addition, the transmission and coordination of the wing flapping, twist, and swing motion can be achieved through the design of a six-bar spatial mechanism based on revolute–revolute–spherical–spherical–spherical–spherical–revolute (RRSS-SSR) to mimic the bionic wing flapping in landing flight.

The design of the flapping wing mechanism is conducted in the following procedure: First, the kinematics of the flapping motion is specified according to the bionic wing motion and required flight performance. Second, the method and mathematical model for the flapping mechanism design are developed. Third, a case study of the flapping wing mechanism is presented to effectively imitate the wing motion. Finally, a prototype model is built based on the flapping mechanism to verify the proposed method and evaluate the effectiveness.

II. FLIGHT CHARACTERISTICS OF BIRDS LANDING

The flapping wing motion of large- and medium-sized birds comprises flapping, twist, and swing, particularly in a short landing process.[15–18] Take the short landing flight of a seagull, as shown in Fig. 1, as an example. The landing process can be divided into four typical stages of wing motion in flapping, twist, and swing. The X–Y–Z coordinate system is set at the mass center of the seagull body O_1. The wing flapping, swing, and twist motion about its root can be expressed in the X–Y–Z coordinates.

The kinematic data from Berg and Biewener[19,20] provided quantitative analysis of landing flight of a pigeon, as illustrated in Fig. 2. The wing tip trajectory in the first, second, and third stages exhibits an "8" shape, and that in the final stage exhibits an open "0" shape [see Fig. 2(a)]. The flapping amplitude, swing amplitude, and pitch angle all satisfy the change relationship of an approximate sine curve in the four stages [see Fig. 2(b)]. When the pigeon's wing flaps to the highest position, the twist angle and swing amplitude both reach a relatively large peak value but not the maximum value. The maximum value lags behind the peak value of the flapping amplitude, and there is a phase relationship. The flapping amplitude of the wing tip gradually increases from 0.1 m to 0.25 m. The pitch angles are all positive, and the amplitude gradually increases from 40° to 50°. The peak pitch angle is ~65° in the first and second stages and ~80° in the third and fourth stages. The designed value of the twist angle can be determined according to one of the four stages. The swing amplitude remains invariant in the four stages and is stable at 0.35 m, and the peak of the swing amplitude is stable at 0.3 m.

To obtain insight into the flapping–twist–swing mechanism of a bird wing, it is necessary to analyze the wing physiological structure. As shown in Fig. 3(a), a bird wing is mainly composed of a skeleton and muscle tendons (red line) wrapped by the patagium (pink area), alula, primaries, and secondaries.[21] The wing skeleton [see Fig. 3(b)] consists of the scapula, shoulder, humerus, elbow, radius, ulna, wrist, metacarpal, phalanges, and thumb. Although the distance from the shoulder to the phalanges is less than half of the wing span, the wing skeleton undertakes all the aerodynamic force generated by the wing. Primaries and secondaries form the main contour of the wing. The primaries are fixed to the metacarpal and phalanges through connective tissue, and the secondaries are fixed to

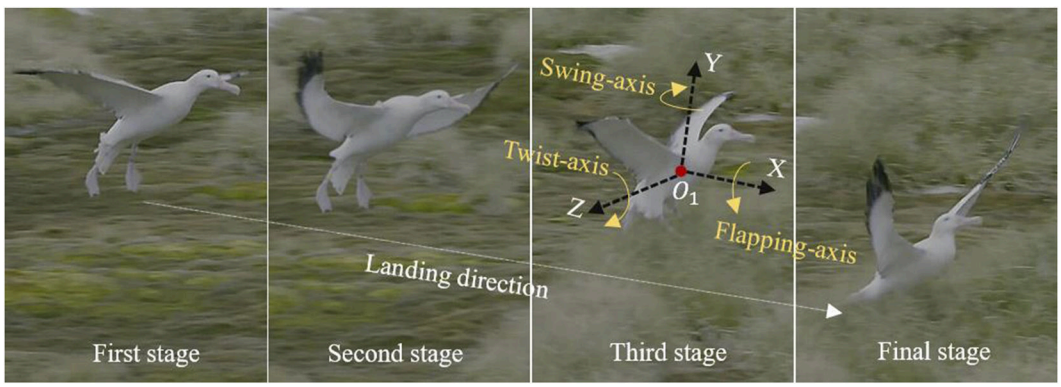

FIG. 1. Characteristics of a seagull during flight landing.

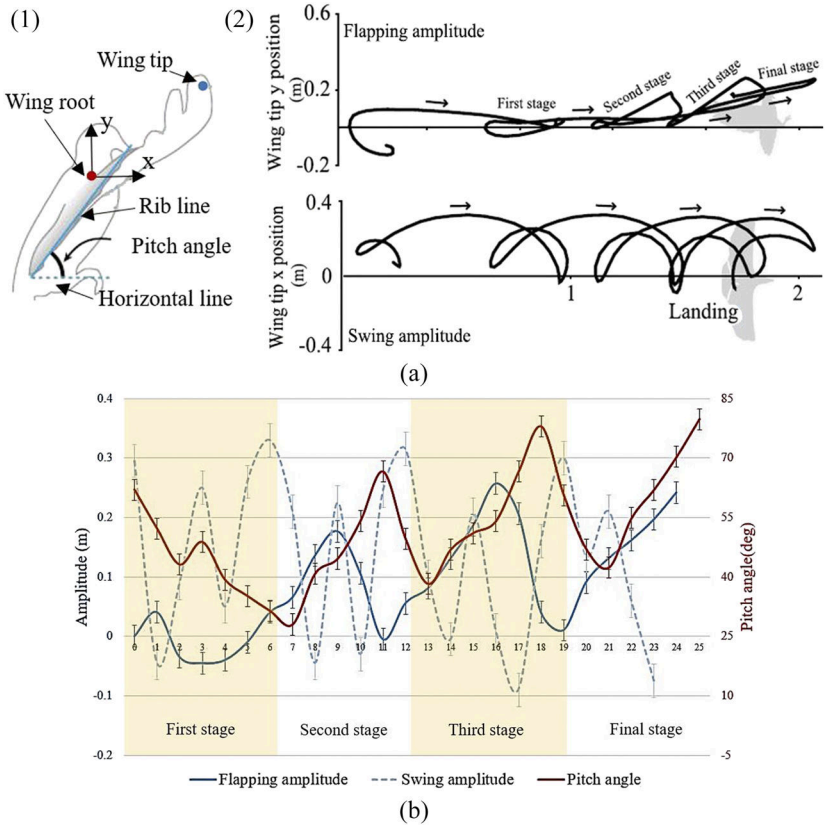

FIG. 2. Trajectory of the wing tips and relationship of the motion parameters during pigeon landing. (a) 1: Definition of the coordinate system of the pigeon's wing; the coordinate system is defined at the wing root, and the angle between the rib line and the horizontal line is defined as the pitch angle. 2: Motion track of the pigeon's wing tip in four stages. (b) General relationship between the pitch angle of pigeon wings and the flapping amplitude and swing amplitude of the wing tips (general relationship between each angle error line is the standard error).

the ulna through connective tissue. Tendons connect the two groups of feathers along the upper surface of the patagium and control the extension of the feathers as the elbow and wrist extend. The gap between the secondaries and the body is filled with feathers [not shown in Fig. 3(a)]. Primaries and secondaries are the main parts for generating aerodynamic force, and they transmit force and torque to the wing skeleton. The torque generated by the primaries travels through the wrist to the end of the radius-ulna, and the torque generated by the secondaries travels through the humerus to the shoulder. Therefore, in the above three joints (shoulder, elbow, and wrist), tendons control the contraction of muscles in different parts to promote the motion of different bones. The shoulder mainly executes flapping and swing, and the elbow and wrist mainly execute stretching and twist, respectively, which form the "flapping–twist–swing" motion. The tendons also increase the twist angle by controlling the secondaries to curve downward. Although the bionic structure of a bird wing demonstrates an ideal mechanism for realizing flapping, twist, and swing, it depends upon the distributed muscle tendon to implement the motion that is not feasible to mimic by the mechanical mechanism.

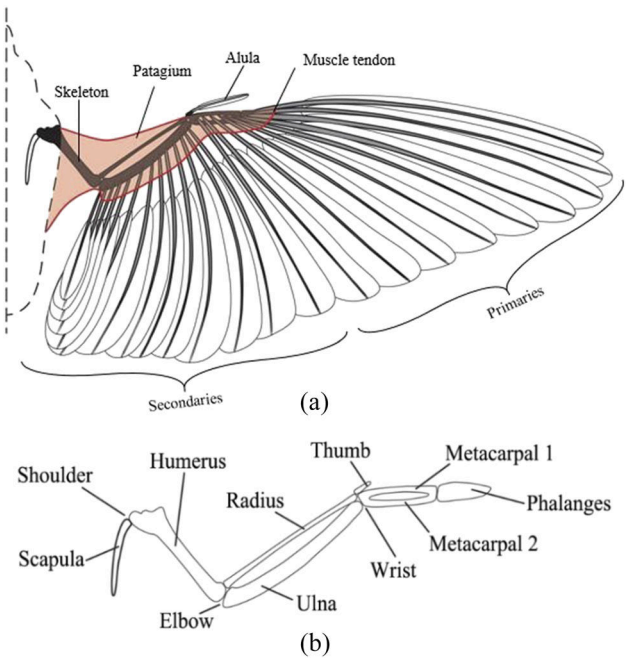

FIG. 3. Wing of large- and medium-sized birds. (a) Wing structure. (b) Wing skeleton structure.

III. FLAPPING WING MECHANISM DESIGN

A. Design inspiration

The movement of the bird wing in three DOFs is driven by the appropriate tendons with multiple drive sources corresponding

to multiple joints. It is not practical to design an efficient and lightweight man-made mechanism to mimic the driving source and achieve the quantity of a bird wing based on a motor driven source. The movement of the flapping mechanism should be designed to mimic the flapping–twist–swing motion. When a rotating motor is used for the driving device, the joints of the flapping wing mechanism should be reduced. In terms of joint type selection, the bird wing shoulder joint and wrist joint are adopted. The shoulder joint realizes flapping and swing, and the wrist joint realizes twist. The main wing bar and rib are the key parts of the flapping wing mechanism. They are connected to the wrist joints to form a T-shaped structure, while the main wing bar and fuselage are connected to shoulder joints. It is necessary to design the transmission mechanism between the main wing bar and the rib under the action of rotation to actively complete the three DOFs coordinated movement of "flapping–twist–swing." The actuating part of the main wing bar drive and the actuating part of the rib drive can be provided with a driving bar. According to the recent studies by Taha *et al.* and Yan *et al.*,[22–24] the coordination of wing flapping, twist, and swing can improve the aerodynamic efficiency. The connecting part between the two driving bars is provided with a phase bar, which is connected to the rotating shaft of the power source. The aforementioned bars constitute a spatial six-bar mechanism.

B. Spatial RRSS-SSR mechanism

1. Design specification

Figure 4 illustrates the RRSS-SSR mechanism design to realize the foregoing transmission and movement presented in this study. The flapping mechanism comprises a "flapping–swing" module and a "twist" module. The two modules are composed of a crank, main drive bar, vice drive bar, main wing bar, rib, and phase bar. This mechanism is capable of transforming the two DOFs movement into a three DOFs flapping wing motion driven by a single power source.[25]

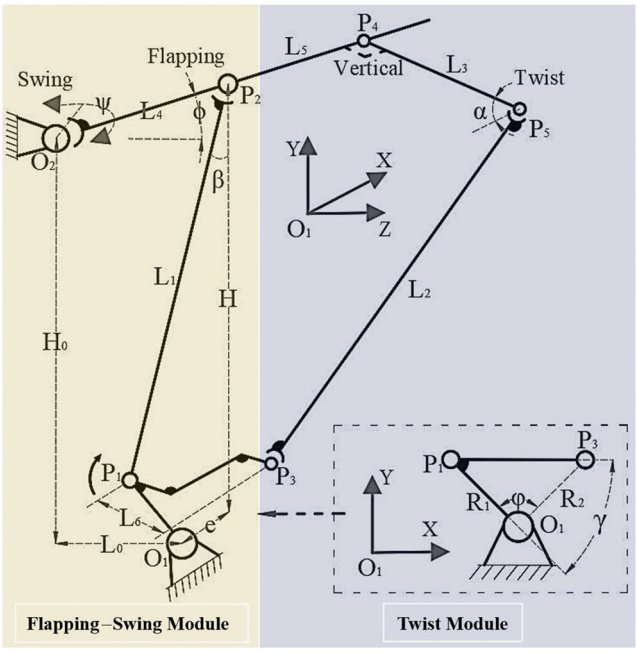

FIG. 4. Spatial RRSS-SSR mechanism: flapping–swing module and twist module.

The origin O_1 of the reference coordinate system is located at the rotation center of the driving shaft mounted to the aircraft body. The flapping wing root is located at the joint O_2 mounted to the body above O_1 with a distance H_0 in the Y-direction. The horizontal distance between O_1 and O_2 is e in the X-axis and L_0 in the Z-axis, respectively. H is the distance between O_1 and P_2 in the Y-axis; R_1 is the length of the crank between joints O_1 and P_1; R_2 is the projection distance between O_1 and P_3 in the XY plane; L_1 is the length of the main drive bar between joints P_1 and P_2; L_2 is the length of the vice drive bar between joints P_3 and P_5; L_3 is the length of the rib between joints P_4 and P_5; O_2P_4 is the inboard main wing bar divided into two parts, L_4 between O_2 and P_2 and L_5 between P_2 and P_4; the phase bar between P_1 and P_3 is of Z-shape with a distance L_6 between the two end joints in the Z-direction; φ is the phase angle between R_1 and R_2 in the XY plane; β is the angle between the main drive bar P_1P_2 and the Y-axis in the XY plane; γ is the installation angle between the phase bar P_1P_3 and the crank O_1P_1 in the XY plane; ϕ and ψ are the flapping and swing angles formed by the main wing bar about the root joint O_2 in the YZ and XZ planes, respectively; α is the twist angle between the X-axis and the rib in the XY plane.

The mechanism consists of the following seven joints: The crank forms the revolute joint with the rack and the main drive bar, respectively. The main wing bar forms the spherical joint with the main drive bar and the rack, respectively. The phase bar is fixed to the crank. The vice drive bar forms the spherical joint with the rib and the phase bar, respectively. The rib and the main wing bar form the revolute joint. When the crank rotates, it drives the main drive bar to perform circular rotation. The main wing bar is limited by the vertical direction of the main drive bar. The main drive bar drives the main wing bar to generate the flapping stroke (YZ plane) and swing stroke (XZ plane) of the wing. Additionally, the rotation of the crank tilts the rib relative to the flapping stroke plane, creating an angle of inclination (i.e., a twist angle) that twists the wing.

To achieve the active control of cooperative "flapping–twist–swing" movement with the three DOFs, the mechanism should have certain parameter constraints. The DOF should be equal to the number of driving sources. The flapping wing mechanism has one rotational source, five moving components, three rotational pairs, four spherical pairs, and two rotational partial DOFs. Therefore, the DOF of the mechanism is expressed as follows:

$$f_1 = 6n - (5n_5 + 3n_3) - f' = 6 \times 5 - (5 \times 3 + 3 \times 4) - 2 = 1. \quad (1)$$

Thus, the RRSS-SSR mechanism has a definite movement.

To determine the flapping, twist, and swing angles of the flapping mechanism, the flapping wing motion equations can be established. The definition, location, and relationship of O_1, O_2, H_0, and L_0 and those basic parameters, as shown in Fig. 5, are identical to those defined in Fig. 4 and used to determine the movement of the flapping mechanism.

The "flapping–swing" module of the flapping mechanism is determined by the four-bar mechanism $O_1P_1O_2P_2$. The distance H between P_2 and O_1 and the angle β vary with the crank rotation and

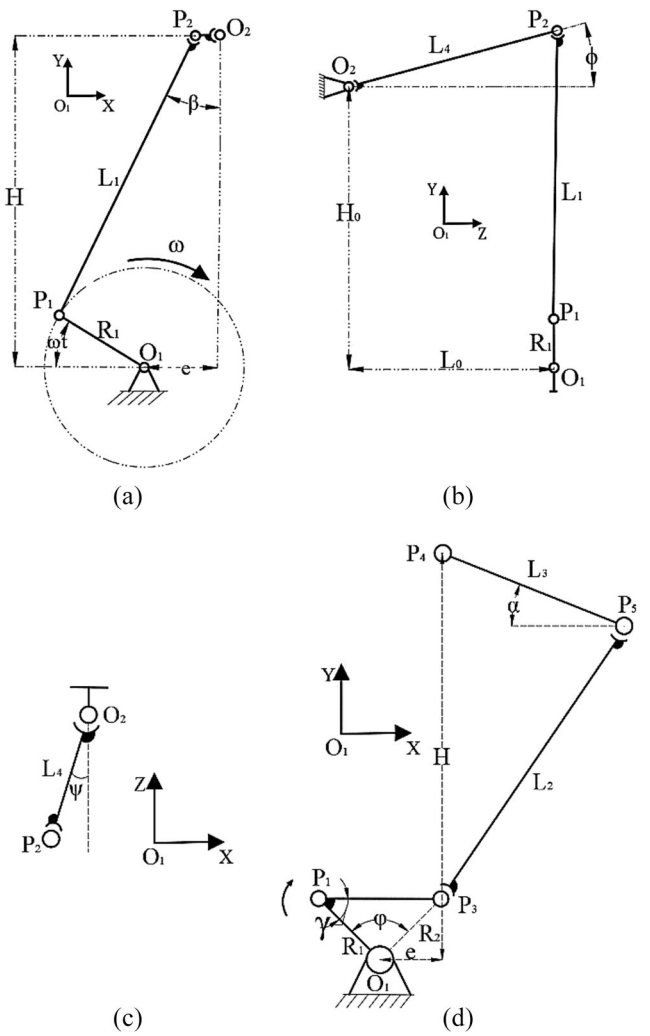

FIG. 5. Flapping, swing, and twist parameters in different views. (a) β angle. (b) Flapping module. (c) Swing module. (d) Twist module.

are expressed below [see Fig. 5(a)]. The clockwise rotation angle ωt of the crank O_1P_1 in the XY plane is negative, and the offset distance e is positive,

$$H = \sqrt{{L_1}^2 - (R_1\cos(\omega t) + e)^2} - R_1\sin(\omega t), \tag{2}$$

$$|\beta| = \arcsin((R_1\cos(\omega t) + e)/L_1). \tag{3}$$

The resulting flapping angle [see Fig. 5(b)] is

$$\phi = \arcsin((H - H_0)/L_4), \tag{4}$$

and the swing angle [see Fig. 5(c)] is

$$\psi = \arctan((R_1\cos(\omega t) + e - L_1\sin\beta)/L_0). \tag{5}$$

The "twist" module of the flapping mechanism is determined by the spatial four-bar mechanism $P_1P_2P_3P_4P_5$ based on the coordinates of the mounting points O_1 and O_2 [see Fig. 5(d)],

$$O_1 = (0, 0, 0), \tag{6}$$

$$O_2 = (e, H_0, -L_0), \tag{7}$$

$$P_1 = (-R_1\cos(\omega t), -R_1\sin(\omega t), 0), \tag{8}$$

$$P_2 = (L_4\sin\psi, H, 0), \tag{9}$$

$$P_3 = (-R_2\cos(\omega t - \varphi), -R_2\sin(\omega t - \varphi), L_6), \tag{10}$$

$$P_4 = (P_{4x}, P_{4y}, P_{4z}), \tag{11}$$

where

$$\begin{cases} P_{4x} = (L_4 + L_5)\sin\psi, \\ P_{4y} = H_0 + (L_4 + L_5)\sin\phi, \\ P_{4z} = P_{2z} + (P_{2z} - O_{2z})\cdot L_5/L_4, \end{cases} \tag{12}$$

$$P_5 = (P_{5x}, P_{5y}, P_{5z}), \tag{13}$$

and

$$\begin{cases} \sqrt{(P_{5x} - P_{4x})^2 + (P_{5y} - P_{4y})^2 + (P_{5z} - P_{4z})^2} = L_3, \\ \sqrt{(P_{5x} - P_{3x})^2 + (P_{5y} - P_{3y})^2 + (P_{5z} - P_{3z})^2} = L_2, \\ (P_5 - P_4)(P_4 - O_2) = 0. \end{cases} \tag{14}$$

The resultant twist angle can be expressed as

$$\alpha = -\arctan((P_{4y} - P_{5y})/(P_{4x} - P_{5x})). \tag{15}$$

2. Mechanism simulation verification

To verify the proposed RRSS-SSR mechanism and the established aircraft model, the data of pigeons in the second stage of landing flight were taken as an example to evaluate the consistence of the bionic design results with the trajectory of the pigeon flapping wing. According to the kinematics of the flapping motion of the pigeon wing, the designed parameters of the mechanism are set as $H_0 = 150$ mm, $L_0 = L_4 = 80$ mm, and $e = 20$ mm. The dimensions of the linkage bars are determined as $R_1 = R_2 = 30$ mm, $L_1 = 185$ mm, $L_2 = 195$ mm, $L_3 = 100$ mm, $L_5 = 15$ mm, and $\varphi = \pi/2$. The flapping amplitude is measured from the wing tip to the wing root. Because the distance from P_2 to the wing tip is half of the wing span, the flapping amplitude and swing amplitude of P_2 are both half of the wing tip and can be calculated based on P_2. The flapping amplitude (see Fig. 6) of the wing tip of the mechanism is 0.13 m, which is close to the flapping amplitude of 0.15 m of the pigeon wing during landing. The twist peak value of 70° in up-stroke and peak value of −20° in down-stroke result in a twist angle with an amplitude of 55°, which is close to the pitch angle amplitude of 50° of the pigeon wings in the second stage of landing. Although the mechanism also produces the swing motion, the amplitude is small and not consistent with the swing trajectory of a pigeon.

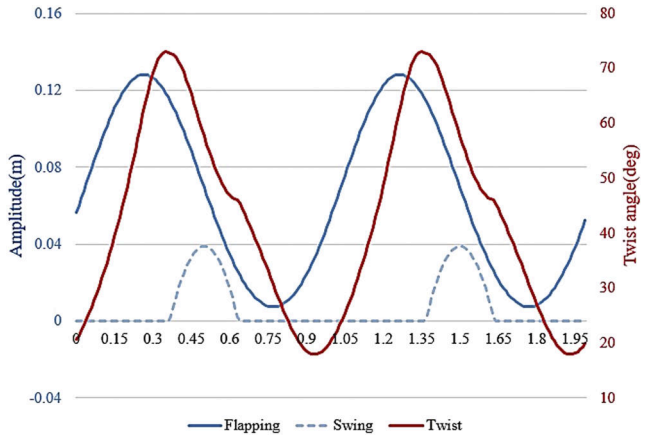

FIG. 6. Comparison of mechanism simulation results and experimental observations.

C. Transmission mechanism engineering

The aforementioned flapping wing motion based on the spatial RRSS-SSR mechanism is consistent with the pigeon wing "flapping–twist" motion in very good approximation. However, it is difficult to mimic the bionic flapping wing motion completely, since the original "flapping–twist–swing" mechanism is simplified for practical application. The number of bars and the installation features were not changed; rather, only the joints were changed. The freedom of the wing root was limited, and only the spherical joints at the wing root to the revolute joints and the revolute joints between the crank and the main drive bar to the spherical joints were changed, as shown in Fig. 7.

The simplified flapping mechanism has one drive source, five moving components, three rotating pairs, four spherical pairs, and two rotational partial DOFs. Therefore, the DOF of the mechanism is

$$f_2 = 6n - (5f_5 + 3f_3) - f' = 6 \times 5 - (5 \times 3 + 3 \times 4) - 2 = 1. \quad (16)$$

The simplified mechanism has a definite movement with movement represented in the following expressions.

Changed parameters [see Fig. 8(a)]:

$$|\beta| = \arccos\left(\sqrt{\left(L_1{}^2 - (R_1\cos(\omega t) + e)^2\right)/L_1{}^2}\right), \quad (17)$$

$$H = |R_1\cos(\omega t) + e|/\tan(|\beta|) - R_1\sin(\omega t). \quad (18)$$

Flapping angle [see Fig. 8(b)] change:

$$\phi = \arcsin((H - H_0)/L_4). \quad (19)$$

P_2 change:

$$P_2 = (e, H, L_4\cos(\phi)). \quad (20)$$

P_{4x} change:

$$P_{4x} = e. \quad (21)$$

Twist angle change:

$$\alpha = -\arctan((P_{4y} - P_{5y})/(P_{4x} - P_{5x})). \quad (22)$$

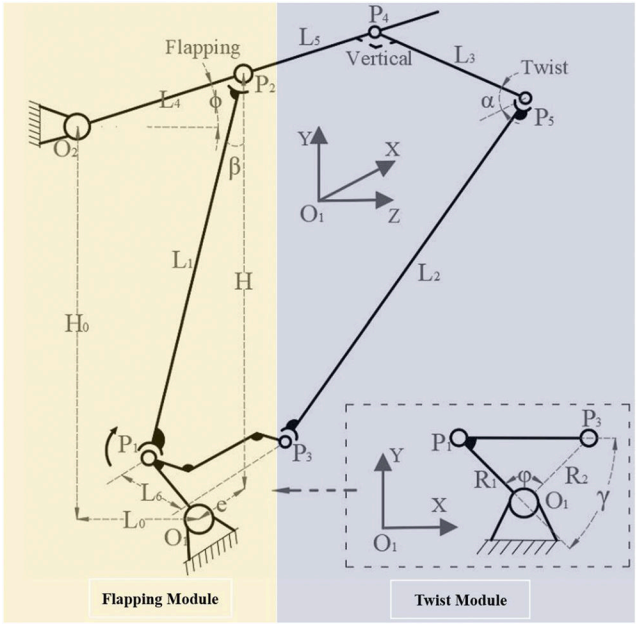

FIG. 7. Engineering mechanism: flapping module and twist module.

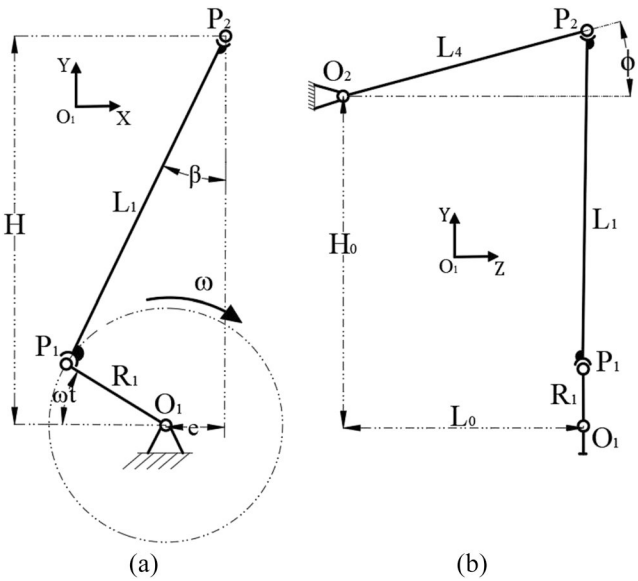

FIG. 8. Changed parameters. (a) β angle. (b) Changed flapping module.

IV. PARAMETER ADJUSTMENT OF ENGINEERING MECHANISM

A. Parameter sensitivity analysis

Because the engineering flapping wing mechanism limits the freedom of swing at the wing root, it is necessary to adjust the mechanism parameters. According to the "flapping and twist" data in the

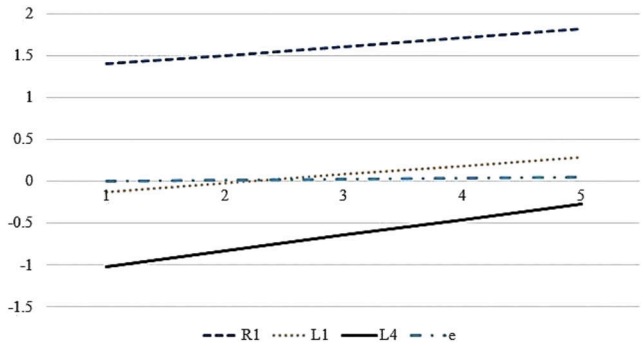

FIG. 9. Analysis of the flapping angle slope.

second stage of pigeon landing flight, we adjust H_0 = 175 mm and L_0 = 80 mm, with respect to other parameters, e = 20 mm, $R_1 = R_2$ = 30 mm, L_1 = 185 mm, L_2 = 188 mm, L_3 = 95 mm, L_4 = 80 mm, $L_5 = L_6$ = 15 mm, and $\varphi = \pi/2$. According to the above motion equations, the effects of the key bars on the flapping angle and twist angle are obtained.

In the flapping module, the key bars that affect the flapping angle are the crank R_1, main drive bar L_1, offset distance e, and part of the main wing bar L_4. The flapping slopes of these four parameters are analyzed (see Fig. 9).

The crank R_1 and L_4 are more sensitive to the flapping angle than the main drive bar L_1 and the offset distance e. R_1 and L_4 should be considered the benchmark design. In the actual manufacturing process, considering the convenience of adjustment, the main drive bar L_1 is taken as the main part to adjust the flapping angle.

In the twist module, the key parameters affecting the twist angle are the main drive bar L_1, vice drive bar L_2, rib L_3, main wing bar ($L_4 + L_5$), cranks R_1, R_2, and phase angle φ. The main drive bar L_1, cranks R_1, R_2, rib L_3, phase angle φ, and vice drive bars L_2, L_5, and L_4 have a gradually decreasing sensitivity to the twist angle (see Fig. 10).

Therefore, in the design of the twist angle, we focus on the phase angle φ, crank R_1, main drive bar L_1, rib L_3, and crank R_2. In the production process, taking into account the convenience of adjustment, the phase angle φ is the main part of the adjustment

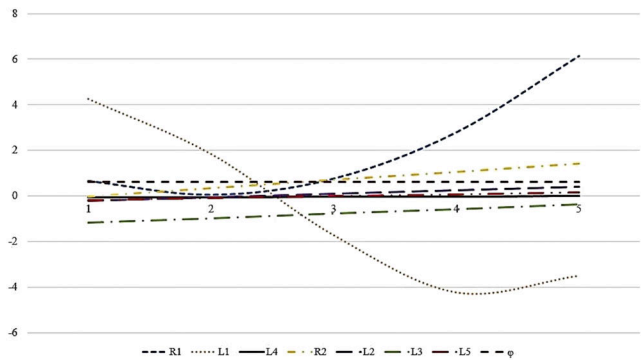

FIG. 10. Analysis of the twist angle slope.

of the twist angle; thus, the phase angle φ executing part can be set as the rotating bar, and the main drive bar L_1 and vice drive bar L_2 can be used as an auxiliary part for the adjustment of the twist angle.

B. Movement of flapping wing

To determine the motion of the wing of the engineering flapping wing mechanism, it is necessary to analyze the motion track characteristics of the wing skeleton under the combination of different sizes and angles of the bar. According to the engineering application of the bar, four flapping modes can be obtained by changing the installation angle of the twist module and the length of the vice drive bar L_2 to ensure the same flapping amplitude.

Flapping wing mode Nos. 1, 2, and 3 are formed by setting $\gamma = 0^\circ$, -45°, and 45°, respectively, and their initial twist angles are in the same direction as the installation angle (the initial angle α_0 is defined as the angle between the rib and the horizontal line in the XY plane when the flapping angle of the wing is 0°). When γ changes from 0° to -45° and the phase angle changes from 180° to 270°, the maximum value of the upper beat and the minimum value of the down beat, as well as the twist amplitude, are consistent. When γ changes from 0° to 45° and the phase angle changes from 180° to 90°, the maximum and minimum values of the upper beat and down beat for twist, as well as the twist amplitude, all decrease, among which the twist amplitude decreases by 29.5%. The twist angle range generated by the flapping in the three aforementioned flapping wing modes is symmetrically distributed; thus, the aerodynamic efficiency is low[26–28] and does not correspond to the flapping and twist motion parameters in the four aforementioned landing stages.

Therefore, to satisfy the high aerodynamic efficiency of the flapping wing aircraft, a small negative twist angle and a large positive twist angle are designed. The phase angle is 90° between the flapping and the twist. The second stage of the pigeon landing is in accordance with a high aerodynamic efficiency. On the basis of flapping wing mode No. 3, L_2 in flapping wing mode No. 4 is reduced to make the initial twist angle $\alpha_0 = -5^\circ$. The phase angle is maintained as 90°, the positive twist angle is 60.5°, the negative twist angle is -13.98°, and the twist amplitude is 74.5°, which is basically the same as that in flapping wing mode No. 3, with a difference of 2.9%. Flapping wing mode No. 4 is close to the wing movement of the pigeon during the second stage of landing. It shows that γ can significantly change the amplitude of the twist angle, and the length of the vice drive bar can change the symmetry of the upper and lower limits of the twist angle. Table I presents the mechanism parameters for the foregoing motion mode.

To visually display the flapping wing trajectory, the flapping wing mechanism corresponding to the four aforementioned movement trajectories is presented (see Fig. 11). Each diagram shows the total stroke of the flapping, and each trajectory diagram is realized as follows: whenever the crank rotates counterclockwise (with a negative bias) for 5°, the main wing bar and rib form projections on the YZ and XY planes, respectively [see Fig. 11(a)].

The track of the main wing bar moves through a fan area, and the trajectories of the rib end exhibit an "8" or "0" shape [see Fig. 11(b)]. In detail, the motion of rib end Nos. 1, 2, and 3 shows similar trajectories to the pigeon wing tip in the first to third stages

TABLE I. Parameters to generate respective flapping patterns.

		α_0 (deg)				α	
No.	γ (deg)	Amplitude	Changed by γ	ϕ (deg)	φ (deg)	Range (deg)	Amplitude (deg)
1	0	0	Passive	51	180	−56.1 to 46.6	102.7
2	−45	−25.2	Passive	51	270	−57.8 to 45.1	102.9
3	45	18.1	Passive	51	90	−35.2 to 37.2	72.4
4	45	−5	Active	51	90	−14.0 to 60.5	74.5

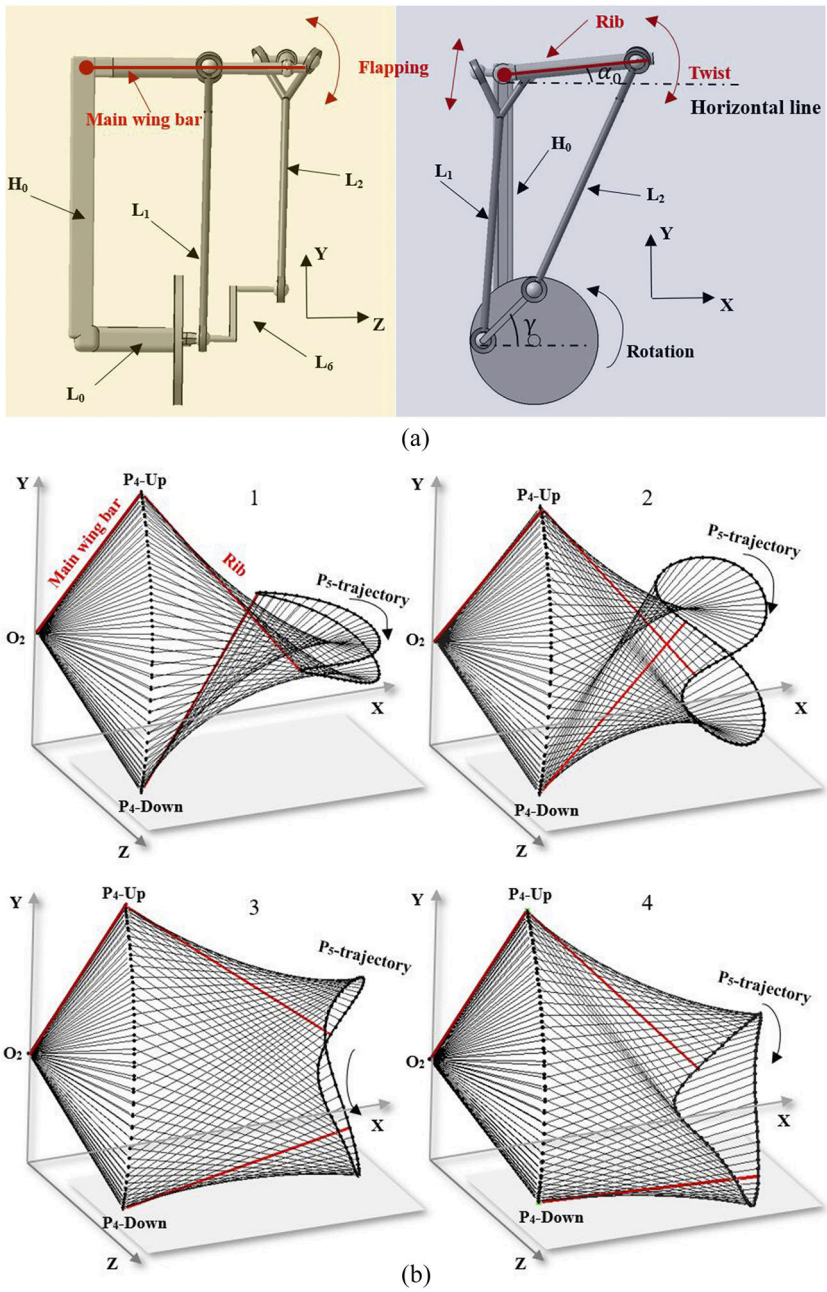

FIG. 11. Movement of the flapping wing. (a) Flapping wing mode test scheme. (b) 1: No. 1; 2: No. 2; 3: No. 3; 4: No. 4.

of landing and the motion of rib end No. 4 shows a similar trajectory to the pigeon wing in the final stage. The trajectories of the rib end in the first, second, and third flapping wing modes all have the same feature: the rib end forms an "8"-shaped trajectory. There is a swing DOF at the rib endings, and we define the angle between the rib and the X-axis in the XZ plane as the swing angle ψ.

Therefore, the end points (the wing tip P_4 and the rib end P_5) that describe the aforementioned trajectory are represented by the following matrix:

$$\begin{pmatrix} P_4 \\ P_5 \end{pmatrix} = \begin{pmatrix} e & H_0 + (L_4 + L_5)\sin\phi & L_4\cos(\phi) + (L_4\cos(\phi) + L_0)\cdot L_5/L_4 \\ P_{5x} & P_{5y} & P_{5z} \end{pmatrix}, \tag{23}$$

where P_5 can be solved by Eq. (14). The angle relationship between P_4 and P_5 is

$$\begin{pmatrix} \phi \\ \alpha \\ \psi \end{pmatrix} = \begin{pmatrix} \arcsin((H - H_0)/L_4) \\ -\arctan((P_{4y} - P_{5y})/(P_{4x} - P_{5x})) \\ \arctan((P_{5z} - P_{4z})/(P_{5x} - P_{4x})) \end{pmatrix}. \tag{24}$$

The swing angle ψ in the three modes in the XZ plane is 20.2°, 19.9°, and 14.2°, respectively, and the swing angle in the fourth flapping wing mode is 19.1°. In the γ range from 0° to −45°, the phase angle varies in the range from 180° to 270° and the swing angle decreases by 0.3° (by 1.5%). In the γ range from 0° to 45°, the phase angle ranges from 180° to 90° and the swing angle decreases by 6° (by 29.7%). The track of the rib ends in flapping wing mode Nos. 2 and 3 based on flapping wing mode No. 1 becomes wider in the Y-direction. In flapping wing mode No. 3, the swing angle increases consistently with that in flapping wing mode Nos. 1 and 2 by reducing the length of the vice drive bar.

V. PROTOTYPE TEST MODEL DESIGN

A. Summary of prototype model

In order to evaluate the performance of the engineering mechanism, a prototype of a double-flapping wing mechanism driven by a single direct-current (dc) brushless motor is constructed (see Fig. 12). This prototype is called SDU-1. The size of the test prototype is set and adjusted according to flapping mode No. 4 of the aforementioned engineering flapping wing mechanism. This flapping mode satisfies the maximum lift required for the aircraft landing. When the wing reaches the maximum flapping speed, the flapping angle and twist angle are close to 0°. Therefore, a benchmark designed size of H_0 = 175 mm (wing root to drive the wheelbase away) is developed. The sizes of the other components are set as follows, according to the benchmark size and designed ideas: R_1 = 31.82 mm, R_2 = 24.24 mm, φ = 90°, L_0 = 80 mm, L_1 = 185 mm, L_2 = 188 mm, L_3 = 95 mm, L_4 = 80 mm, L_5 = 50 mm, L_6 = 15 mm, and e = 20 mm. The wingspan is 0.9 m, and the maximum chord length is 0.2 m. The fuselage of the test prototype includes installation points 1 and 2. Installation point 1 mainly supports the wing, and installation point 2 is used to install the reduction gear and the brushless dc motor. The double-flapping wing mechanism moves between installation points 2 and 1.

A carbon fiber bar, a carbon fiber board, an aluminum pipe, an aluminum plate, SA4T/K spherical bearings, gears, and 3D printed components are used to construct the prototype. A carbon fiber plate is used to construct the prototype body, aluminum tube and the combination of the spherical bearing used in the main drive bar assembly and vice driving bar, aluminum plate used to cut into phase bar, crank and main wing bar sleeve and rib sleeve made by 3D printing photosensitive resin. During the assembly process, the meshing between gears is adequate for the transmission power of the brushless dc motor. The connection of the crank and phase bar is fixed by thread glue. The prototype adopts a brushless dc motor as the power source. The motor speed constant KV is 3600 rpm/v, and the reduction gear transmission ratio G is 11.

B. Installation of twist module

The twist module is installed on one side of the flapping module through a bolt at one end of the phase bar [see Fig. 13(a)]. The twist module length adjustment principle is presented [see Fig. 13(b)]. Considering that changes in the key bar size affect the operability of the prototype, it is more convenient to adjust the length of the main drive bar, the vice drive bar, and the phase bar. For example, the two ends of the vice drive bar are provided with internal thread holes, to facilitate connection with the spherical bearing via external thread. The extendable vice drive bar is rotated

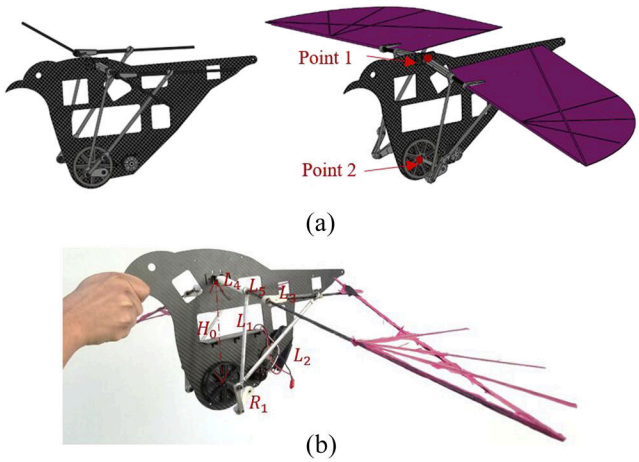

FIG. 12. Prototype. (a) CAD model with patagium and no patagium. (b) Physical model with no patagium.

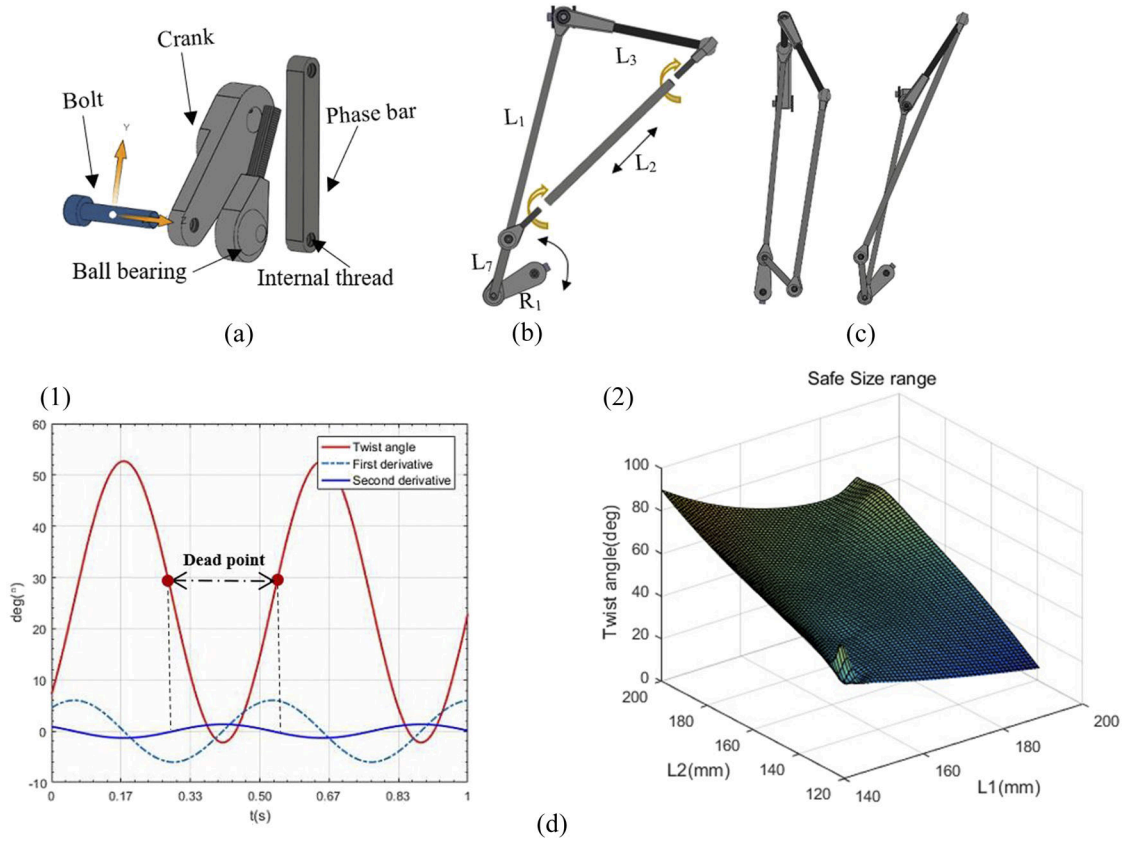

FIG. 13. Installation principle of the twist module. (a) Installation mechanism. (b) Bar length adjustment (taking the vice drive bar as an example) and installation angle adjustment. (c) Bar position to the extreme dead point. (d) 1: Dead point position. 2: Safe size envelope diagram.

along the direction in the figure; otherwise, the length of the vice drive bar is reduced. The installation angle of the twist module can be adjusted by rotating the phase bar around the bolt to the set angle.

Owing to the certain deviation between the size obtained in the process of physical assembly and the designed size, two dead spots of flapping wing movement appear in extreme cases [see Fig. 13(c)]. Therefore, the approximate dead point position on the curve is divided [see Fig. 13(d)], and the second derivative of the change trend of the twist angle is calculated. When the second change is 0°, 20°–40° is the range where the dead point can easily appear. The safe range of the total amplitude of the twist angle about the main drive bar and the vice drive bar is given. In the range of 100 mm–200 mm for the adjustable size of the main drive bar and the vice drive bar, the upper limit of the total amplitude of the twist angle can reach 90° and the lower limit can reach 20°.

VI. RESULTS AND DISCUSSION

A. Establishment of experimental platform

To capture the motion of the flapping wing in the experiment, the test model was mounted to a load cell (ATI-Nano25) that was located within a 3 × 3 × 2 m^3 test space, a motion-capture device with 12 infrared cameras (OptiTrack Prime 13) was set around the test model, and the measured force and infrared tracker data were transferred to a computer for data processing and analysis, as shown in Fig. 14(a). To reflect the key spatial points of the flapping wing in motion, six fluorescent ball joints were mounted at the wing tip, the leading and trailing edges of the rib, and the body along the central line [see Fig. 14(b)]. The model connected to the load cell was mounted on a Pi-shaped steel frame that was mounted on a test bench, as shown in Fig. 14(c). The test model with and without the wing patagium was tested to measure the total force and inertial force generated by flapping wing movement [see Fig. 14(d)].

B. Experimental results and analysis of movement

The flapping angle change was obtained via the model experiment (see Fig. 15). The flapping amplitude was 54° (32° and −22° for the upper and down beats, respectively). Compared with the theoretical calculation value of the flapping angle amplitude (48°: upper beat, 30°; down beat, −18°) based on the design parameters, the experimental value had a 6° error (relative error of 12.5%). The twist angle amplitude measured in the experiment was 42° (upper beat, 47°; down beat, 5°), and the calculated twist angle amplitude

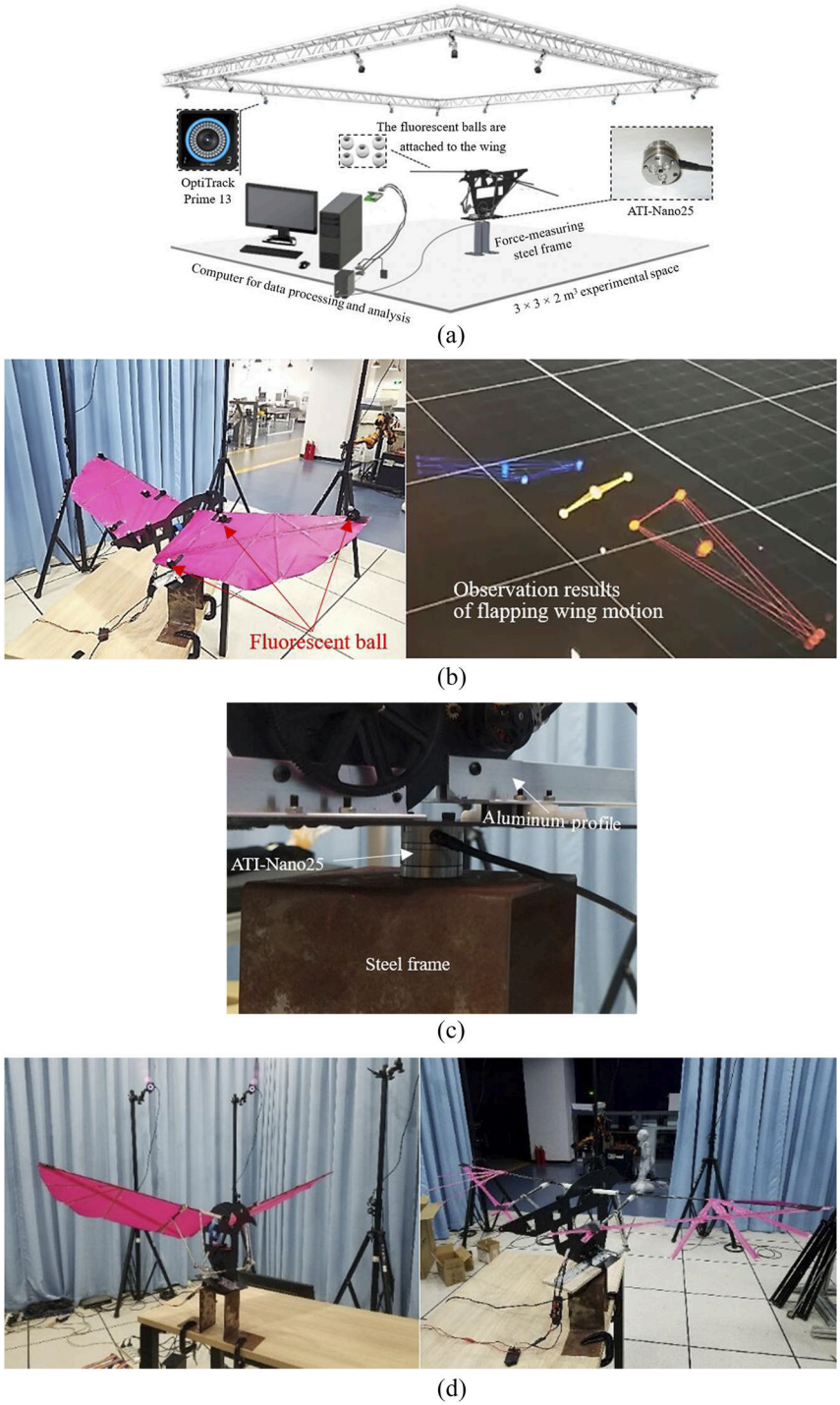

FIG. 14. (a) Experimental device for observing flapping wing movement and longitudinal forces. (b) Fluorescent ball marking the position and observation results of motion. (c) Installation of the sensor. (d) Field test diagram of the flapping wing model (with and without the wing patagium).

was 58° (upper beat, 58°; down beat, 0°). There was a 16° error (relative error of 27.6%) between the experimental and theoretical values for the twist angle amplitude. The experimentally measured swing angle amplitude was 40° (upper beat, 35°; down beat, −5°), and the theoretical swing angle amplitude was 45° (upper beat, 41°; down beat, −4°). There was a 5° error (relative error of 11.1%) between the experimental and theoretical values for the swing angle amplitude.

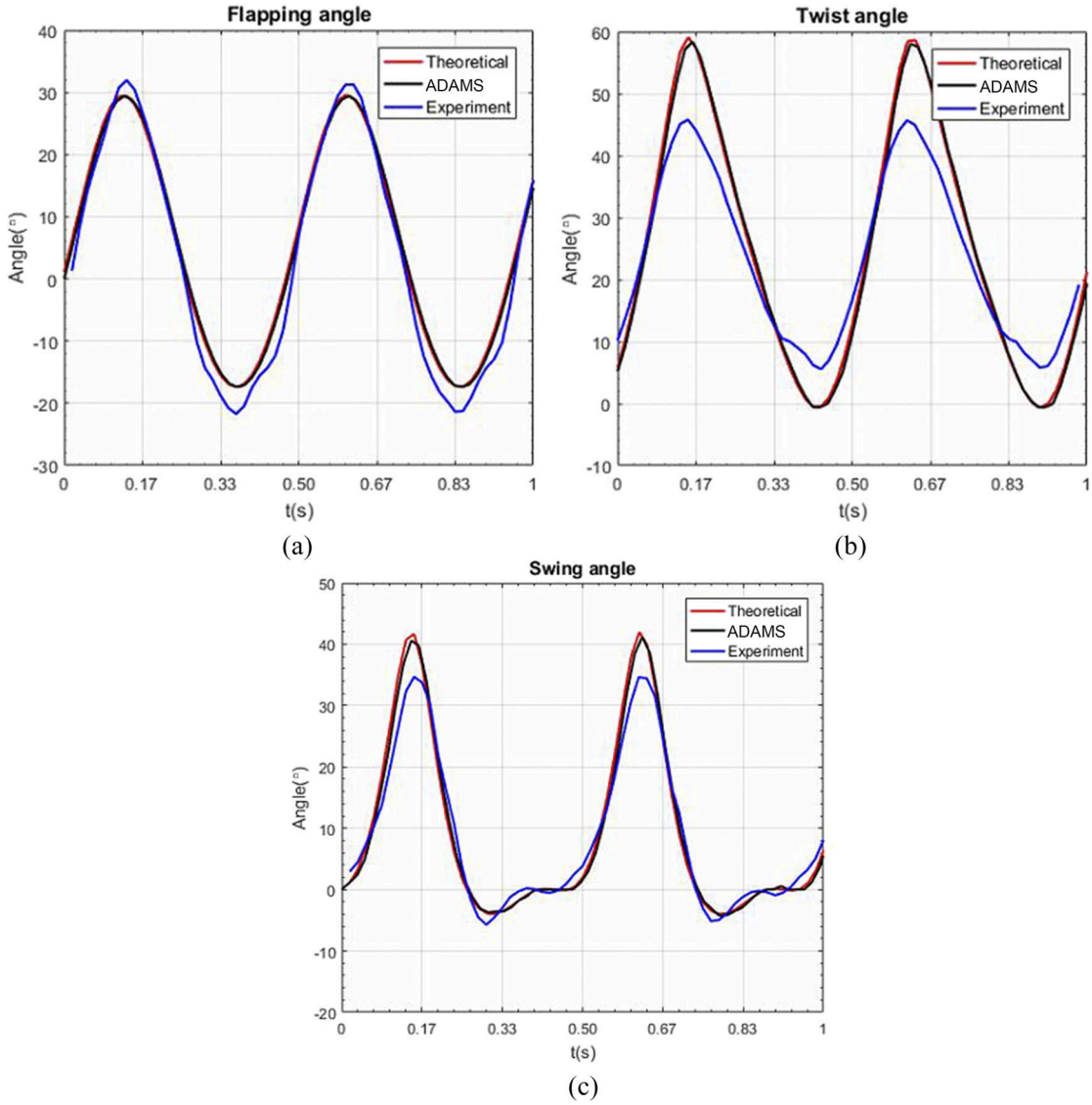

FIG. 15. Comparison between experimental data of prototype, theoretical model calculation results, and ADAMS numerical calculation results. (a) Flapping angle. (b) Twist angle. (c) Swing angle.

Regarding error analysis for the flapping angle, owing to the rigid body setting adopted by the developed mathematical motion model and the numerical model established using ADAMS, the main wing bar does not undergo elastic deformation during flapping. However, the physical material of the main wing bar is a carbon rod. In the process of flapping, the main wing bar is easily subjected to elastic deformation, increasing the amplitude of the flapping angle.

Regarding the twist and swing angles, the twist module integrates the twist and swing angle parameters; therefore, the assembly error easily occurs in a real assembly process, particularly in the rubber thread fixed parts. The actual phase angle was 70°, compared with the design value of 90°. By importing the actual phase difference into the theoretical model, the twist and swing angles were corrected relative to the actual values (see Fig. 16). The amplitude of the modified theoretical twist angle was 43° (relative error of 2.3%). The amplitude of the modified theoretical swing angle was 36° (relative error of 11.1%).

In terms of the movement characteristics, the experimental data and theoretical calculation results of the prototype (taking the ADAMS simulation as an example) both exhibit a consistent variation trend of each motion parameter (see Fig. 17), satisfy the prototype in the flapping to the highest point, and satisfy a large twist angle. When the down beat reaches the maximum flapping speed, the flapping angle and twist angle are close to 0°.

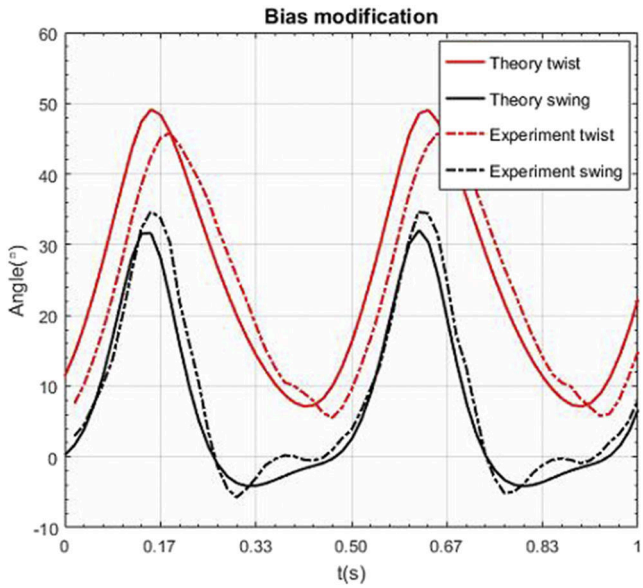

FIG. 16. Bias modification.

C. Experimental results and analysis of vertical force

The theoretical and practical vertical force characteristics of the test prototype at 2.1 Hz without air flow were analyzed. The first test involved the vertical force received by the prototype in the case of the wing patagium (the vertical force included the inertial force received by the wing patagium). The second test involved the inertial force under the condition of no wing patagium, compared with the theoretical calculation. The wingspan of the prototype was 1 m, the rib length was 25 cm, and the area of a single wing surface was 817.55 cm^2. Table II shows the weight of each part of the prototype.

The inertial force without the wing patagium and the total force with the wing patagium are presented (see Fig. 18). The amplitude of the inertial force is ~1.6 N. The maximum value of the upper beat is 0.9 N, and the maximum value of the down beat is approximately −0.7 N. The amplitude of the inertial force calculated theoretically is also 1.6 N, where the maximum value of the upper beat is 0.85 N and the maximum value of the down beat is −0.75 N. The experimental results are close to the theoretical calculation results of the inertial force amplitude, and the slight deviation is mainly due to the inertial force error caused by the deviation between the theoretical parameters and the experimental data of the flapping wing movement.

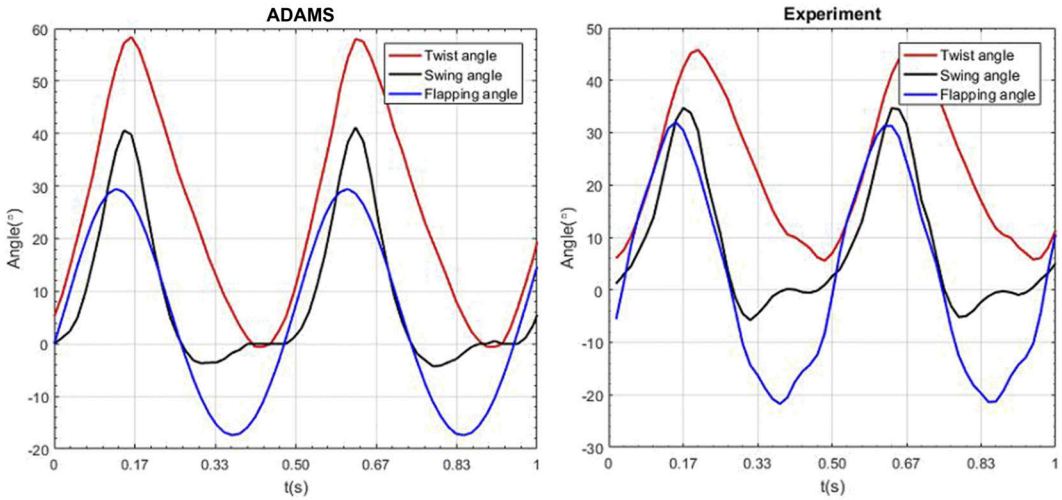

FIG. 17. (a) Motion relation under theoretical simulation. (b) Motion relation under experimental conditions.

TABLE II. Unit weight (g).

Unit	Weight	Unit	Weight	Unit	Weight
Main wing bar	12.35	Main wing bar sleeve	11.15	Ball bearing	5.46
Rib sleeve	2.77	Rib	5.06	Main drive bar	9.53
Vice drive bar	8.8	Bearing	1.72	Patagium	9.64
Phase bar	3.28	Crank	4.33		

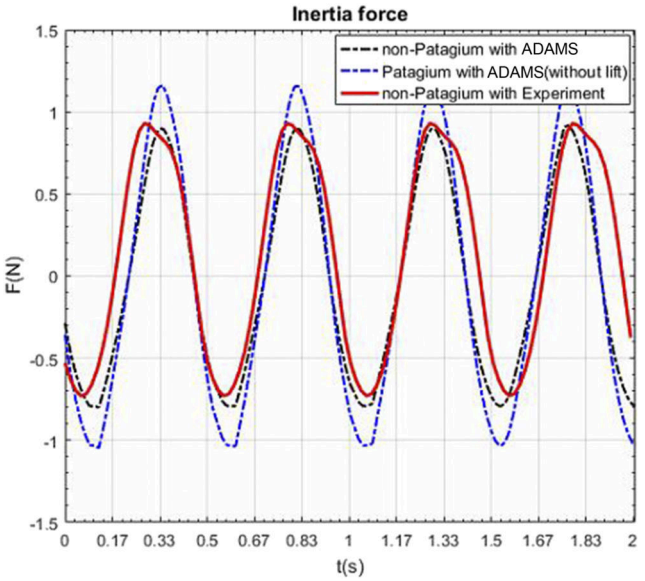

FIG. 18. Inertial force of the prototype without the wing patagium, total force of the prototype with the wing patagium, and calculation results of theoretical vertical force.

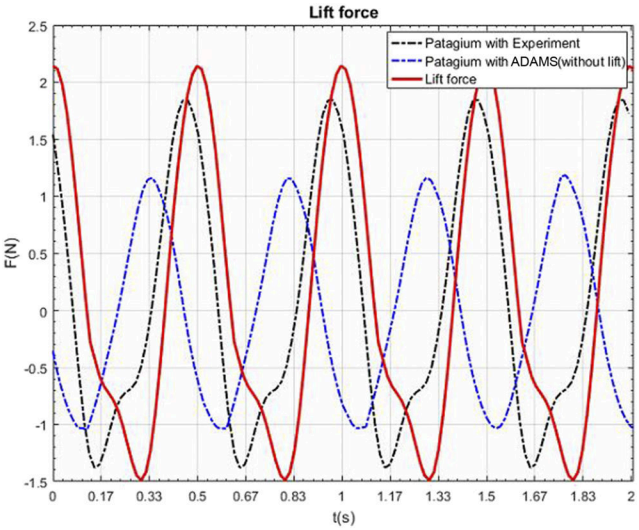

FIG. 19. Lift of the prototype.

The maximum relative error of the upper beat is 5.9%, and the maximum relative error of the down beat is 6.7%.

Because the wing patagium accounts for 35.6% of the wing weight, it is necessary to consider its inertial force. It is difficult to measure the inertial force of the wing patagium in the prototype, and the wing patagium induces a lifting force. Therefore, the inertial force with the wing patagium is calculated theoretically. According to the calculation, the amplitude of inertial force with the wing patagium is ~2.2 N, where the upper-beat value is ~1.15 N and the down-beat value is approximately −1.05 N. After subtraction, the theoretical inertial force of the wing patagium in the flapping stroke of the prototype is ~0.6 N, and the inertial force contributed by the wing patagium accounts for 27.3%.

For estimating the lift of the prototype, the total vertical force of the prototype with the wing patagium is measured experimentally (see Fig. 19). Then, the theoretical calculation value of the total inertial force of the prototype with the wing patagium is subtracted, yielding a maximum positive lift of 2.1 N for the down beat and yielding a maximum negative lift of 1.5 N for the upper beat.

According to an analysis of the relationship between the prototype inertial force and the motion (see Fig. 20), the inertial force peak occurs at two locations: the top and bottom of the flapping wing. At these points, the acceleration is maximized with the prototype in the vertical direction; the change in velocity and the inertial

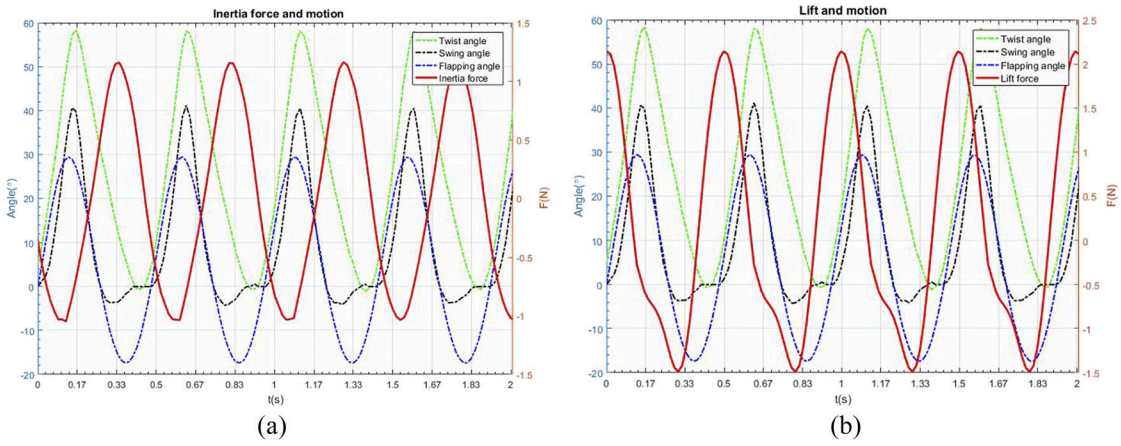

FIG. 20. (a) Relationship of flapping wing movement and inertia force. (b) Relationship of flapping wing movement and lift of the prototype.

force are minimized with flapping in the horizontal position, and the acceleration in the vertical direction is minimized. According to an analysis of the relationship between the lift and the motion of the prototype, when the prototype is flapping to the flat position, the effective area of the flapping wing is maximized, and its lift is maximized according to the lift formula.

VII. CONCLUSIONS

A flapping mechanism capable of producing a three DOFs motion (flapping, twist, and swing) was developed based on the study of the flapping characteristics of a bird flapping wing in landing flight. This new flapping wing mechanism can transform a rotating movement from a power source to a coordinative motion with the three DOFs output. The design is based on the RRSS-SSR joint spatial six-bar flapping wing mechanism, and each output has a definite motion to mimic a completely bionic flapping wing mechanism. For the practical application, the mechanism is simplified to a system of two DOFs motion. The number of bars and installation features were not changed; rather, only the joint connection features were changed. The freedom at the wing root was limited, and only the spherical joint at the wing root to the revolute joint and the rotation joint between the crank and the main drive bar to the spherical joint were changed. Thus, the mechanism of the test model was simplified to keep the "flapping–twist" motion only. According to this mechanism, a physical model with a wingspan of 0.9 m was constructed to realize the wing posture of a bird landing.

A parameter sensitivity analysis of the flapping wing mechanism revealed that the sensitivity of the crank R_1 and L_4 to the flapping angle was higher than that of the main drive bar L_1 and offset distance e. However, the main drive bar L_1 was taken as the main part of the flapping angle adjustment in the actual manufacturing process, considering the difficulty of adjusting the flapping angle with the crank R_1 and part of the main wing bar L_4. The sensitivity to the twist angle decreased in the following order: main drive bar L_1, cranks R_1, R_2, rib L_3, phase φ (can be replaced by the installation angle γ), and vice drive bars L_2, L_5, and L_4. In the actual manufacturing process, the convenience of adjusting the twist angle is considered, with the phase angle as the main part of the adjustment of the twist angle. The main drive bar L_1 and vice drive bar L_2 can be used as an auxiliary part for the adjustment of the twist angle. Additionally, L_2 affects the symmetry degree of the upper and lower limits of the twist angle. The track of the rib ending exhibits an "8" and "0" shape when the installation angle ($\gamma = 0°$) changes to $-45°$ and $45°$, respectively. Additionally, the track of the rib ending changes from narrow to wide along the Y-direction. Based on the flapping wing mode of $\gamma = 45°$, it can increase the swing amplitude to reduce L_2 of the vice drive bar.

According to the prototype of the engineering flapping wing mechanism, the key bar and installation angle that significantly affect the flapping wing movement were set through screw connections. An analysis was performed to avoid the dead point in the process of prototype movement, revealing that the dead point easily appears in the range of 20°–40° of the twist angle of the rib. Additionally, the upper limit of the twist angle can reach 90° and the lower limit can reach 20° within the adjustable size range from 100 mm to 200 mm of the main drive bar and the vice drive bar. These results potentially provide useful guidance for the design of bionic flapping wing mechanisms of a flapping wing aircraft for short landing flight.

ACKNOWLEDGMENTS

The authors disclosed receipt of the following financial support for the research, authorship, and/or publication of this article: This study was supported by the National Key R&D Program of China (Grant No. 2018YFB1305400) and the National Natural Science Foundation of China (Grant Nos. 61673246 and 81301294).

The authors declare that there is no conflict of interest regarding the publication of this paper.

DATA AVAILABILITY

The data that support the findings of this study are available from the corresponding author upon reasonable request.

REFERENCES

[1] S. P. Sane and M. H. Dickinson, "The control of flight force by a flapping wing: Lift and drag production," J. Exp. Biol. **204**(Pt 15), 2607–2626 (2001).

[2] T. J. Muller, *Fixed and Flapping Wing Aerodynamics for Micro Air Vehicle Applications* Progress in Astronautics and Aeronautics (AIAA, 2001), p. 195.

[3] S. Ho, H. Nassef, N. Pornsinsirirak, Y.-C. Tai, and C.-M. Ho, "Unsteady aerodynamics and flow control for flapping wing flyers," Prog. Aerosp. Sci. **39**(8), 635–681 (2003).

[4] T. N. Tai, Y. C. Tai, C. M. Ho *et al.*, "Microbat: A palm-sized electrically powered ornithopter," in Proceedings of the NASA/JPL Workshop on Biomorphic Robotics, 2001.

[5] K. Y. Ma, S. M. Felton, and R. J. Wood, "Design, fabrication, and modeling of the split actuator microrobotic bee," in *IEEE/RSJ International Conference on Intelligent Robots and Systems* (IEEE, 2012).

[6] M. Keennon, K. Klingebiel, and H. Won, "Development of the nano hummingbird: A tailless flapping wing micro air vehicle," in *AIAA Aerospace Sciences Meeting Including the New Horizons Forum and Aerospace Exposition* (AIAA, 2012.

[7] See https://www.festo.com.cn/group/zh/cms/10238.htm for SmartBird Bird flight deciphered.

[8] J. Yan, T. Su, S. A. Avadhanula, M. Sitti, M. H. Dickinson, R. S. Fearing, and J. Birch, "Wing transmission for a micromechanical flying insect," J. Micromechatronics **1**(3), 221–237 (2001).

[9] A. T. Conn, S. C. Burgess, and C. S. Ling, "Design of a parallel crank-rocker flapping mechanism for insect-inspired micro air vehicles," Proc. Inst. Mech. Eng., Part C **221**(10), 1211–1222 (2007).

[10] M. Balta, K. A. Ahmed, P. L. Wang, J. M. McCarthy, and H. E. Taha, "Design and manufacturing of flapping wing mechanisms for micro air vehicles," AIAA Paper No. 2017-0509, 2017.

[11] P. L. Wang and J. J. Michael McCarthy, "Design of a flapping wing mechanism to coordinate both wing swing and wing pitch," J. Mech. Rob. **10**(2), 025003-1–025003-6 (2018).

[12] G. N. Sandor, L. J. Xu, and S. P. Yang, "Computer-aided synthesis of two-closed-loop RSSR-SS spatial motion generator with branching and sequence constraints," Mech. Mach. Theory **21**(4), 345–350 (1986).

[13] C. H. Chiang, Y.-N. Yang, W. H. Chieng, and D. A. Hoeltzel, "Four-position synthesis for spatial mechanisms with two independent loops," Mech. Mach. Theory **29**(2), 265–279 (1994).

[14] W.-Y. Chung, "Synthesis of spatial mechanism UR-2SS for path generation," J. Mech. Rob. **7**(4), 041009 (2015).

[15] See https://www.scientificamerican.com/article/flying-on-flexible-wings/ for Flying on Flexible Wings.

[16]B. Tobalske and K. Dial, "Flight kinematics of black-billed magpies and pigeons over a wide range of speeds," J. Exp. Biol. **199**(Pt 2), 263–280 (1996).
[17]M. N. O. Davies and P. R. Green, "Optic flow-field variables trigger landing in hawk but not in pigeons," Naturwissenschaften **77**(3), 142–144 (1990).
[18]H. I. Fisher, "The landing forces of domestic pigeons," Auk **73**(1), 85–105 (1956).
[19]A. M. Berg and A. A. Biewener, "Wing and body kinematics of takeoff and landing flight in the pigeon," J. Exp. Biol. **213**(10), 1651–1658 (2010).
[20]A. M. Berg and A. A. Biewener, "Kinematics and power requirements of ascending and descending flight in the pigeon," J. Exp. Biol. **211**(7), 1120–1130 (2008).
[21]C. Pennycuick, *Modelling the Flying Bird* (Academic Press, 2008), Vol. 5, pp. ix–x.
[22]H. E. Taha, S. Tahmasian, C. A. Woolsey, A. H. Nayfeh, and M. R. Hajj, "The need for higher-order averaging in the stability analysis of hovering, flapping-wing flight," Bioinspiration Biomimetics **10**(1), 016002 (2015).
[23]H. E. Taha, A. H. Nayfeh, and M. R. Hajj, "Effect of the aerodynamic-induced parametric excitation on the longitudinal stability of hovering MAVs/insects," Nonlinear Dyn. **78**(4), 2399–2408 (2014).
[24]Z. Yan, H. E. Taha, and M. R. Hajj, "Effects of aerodynamic modeling on the optimal wing kinematics for hovering MAVs," Aerosp. Sci. Technol. **45**, 39–49 (2015).
[25]J. W. Gerdes, S. K. Gupta, and S. A. Wilkerson, "A review of bird-inspired flapping wing miniature air vehicle designs," J. Mech. Rob. **4**(2), 021003-1–021003-11 (2012).
[26]J.-M. Miao and M.-H. Ho, "Effect of flexure on aerodynamic propulsive efficiency of flapping flexible airfoil," J. Fluids Struct. **22**(3), 401–419 (2006).
[27]I. Tuncer, R. Walz, and M. Platzer, "A computational study on the dynamic stall of a flapping airfoil," in 16th AIAA Applied Aerodynamics Conference (AIAA, 1998).
[28]C. Si, L. Hao, G. Shijun *et al.*, "Unsteady aerodynamic model of flexible flapping wing," Aerosp. Sci. Technol. **80**, 354–367 (2018).

2020-06-12

Design and experiment of a bionic flapping wing mechanism with þÿ f l a p p i n g t w i s t s w i n g m o t i o n b a single rotation

Ji, Bing

AIP Publishing

Ji B, Zhu Q, Guo S, et al., (2020) Design and experiment of a bionic flapping wing mechanism þÿ w i t h f l a p p i n g t w i s t s w i n g m o t i o n b a s e d o n a s i n g l e r o t a t i o n . A I P A d v a n c e 6, 2020, Article number 065018

https://doi.org/10.1063/5.0008792